THE PENNSYLVANIA STATE UNIVERSITY
SCHREYER HONORS COLLEGE

DEPARTMENT OF METEOROLOGY AND ATMOSPHERIC SCIENCE

Detecting Tropical Cyclone Secondary Eyewalls with a Microwave-Based Scheme

ALEX ALVIN CHEUNG
SPRING 2022

A thesis
submitted in partial fulfillment
of the requirements
for a baccalaureate degree
in Meteorology
with honors in Meteorology

Reviewed and approved* by the following:

Steven Greybush
Associate Professor of Meteorology
Thesis Supervisor

Jenni L. Evans
Professor of Meteorology and Atmospheric Science
Thesis Supervisor

Raymond G. Najjar Jr.
Professor of Oceanography
Honors Adviser

* Electronic approvals are on file.

ABSTRACT

Intense tropical cyclones (TCs) often form secondary eyewalls, triggering a process known as an eyewall replacement cycle (ERC). This can lead to short-term fluctuations in intensity and an increase in the size of the TC wind field. When occurring near landfall, the short-term variations can dramatically alter coastal watch, warning, and storm surge forecasts, potentially altering pre-storm preparation plans, including evacuations. However, documenting these events can be a time-consuming, subjective, and sometimes difficult task. Here, we use 89 –92 GHz microwave imagery from the NOAA Cooperative Institute for Research in the Atmosphere's Tropical Cyclone PRecipitation, Infrared, Microwave, and Environmental Dataset (TC PRIMED) to develop image-based variables to identify concentric structures related to deep convection. The image-based variables are combined with various environmental and storm variables (e.g, deep-layer shear magnitude, current maximum wind speed, 24-h difference in radius of 5 kt (1 kt = 0.514 m s^{-1}) winds, and 24-h difference in infrared brightness temperature), to create a probabilistic secondary eyewall classification scheme using a machine learning classifier (linear discriminant analysis). This classification scheme is trained and tested using subjectively created secondary eyewall labels (2016–2019) of storms from the North Atlantic, East Pacific, West Pacific, and Southern Hemisphere basins. We trained the classifier using 36 storms and retained 16 storms for testing. From the classifier output, we calculate the probability of detection, false alarm ratios, skill scores, and bias ratio for various probability thresholds. Using the best default probability threshold (50%), the model produced a secondary eyewall probability of detection of about 64% with a false alarm ratio of 34% and a Peirce's Skill Score of 0.52, indicating fair skill in the model.

TABLE OF CONTENTS

LIST OF FIGURES

LIST OF TABLES

ACKNOWLEDGEMENTS

First and foremost, I would like to thank my amazing mentor, Christopher Slocum (NOAA Center for Satellite Applications and Research). Chris spent countless hours working with me both in-person in Fort Collins, CO and on Slack. The skills I gained from this project tremendously helped me develop research skills that will prepare me for graduate school. Second, I would like to thank John Knaff (NOAA Center for Satellite Applications and Research). John was deeply involved in this project and provided extremely important feedback for many aspects of this project. Outside of this project, John and Chris also provided me valuable feedback and insightful knowledge regarding choosing a graduate school. I will be returning to Fort Collins, CO following my graduation to continue this project and I am looking forward to working with John and Chris again. At Penn State, I would like to thank Dr. Steven Greybush for his mentorship over the last two years. Through three different projects, including my first ever research experience, I gained valuable research skills that would not have been possible without his dedication towards helping me grow as a scientist. Lastly, I would also like to thank Dr. Jenni Evans for her support and valuable feedback on this project. This work has been supported by the National Science Foundation Research Experiences for Undergraduates Site in Earth System Science at Colorado State University under the cooperative agreement No. AGS-1950172. The scientific results and conclusions, as well as any views or opinions expressed herein, are those of the author(s) and do not necessarily reflect those of NOAA or the Department of Commerce.

Chapter 1

Introduction

Tropical cyclones (TCs) are the deadliest and costliest type of natural disaster. Of the 22 billion-dollar United States disasters in 2020, seven were TCs, resulting in the death of 262 people (NOAA 2022). The potential damage of a TC increases dramatically with increasing wind speed and wind field size, hence even small changes in these quantities can lead to vastly different outcomes (Nordhaus 2006; Powell and Reinhold 2007). While TC intensity forecasts are slowly improving (DeMaria et al. 2014), forecasts for intense TCs (max wind speed > 96 kt; 1 kt = 0.514 m s^{-1}) still need to be improved to minimize losses. One of the sources of uncertainty in the forecast of both intensity and the wind field for forecasting intense TCs is secondary eyewall formations (SEF), an organized semi-symmetric cluster of thunderstorms surrounding the inner thunderstorms associated with the TC eye. SEFs are part of a process known as an eyewall replacement cycle (ERC; Willoughby et al. 1982) and are not easily predicted because the physics for their cause is still uncertain. ERCs are a very important area of study because TC characteristics during this process can change in the following ways: (1) sudden fluctuations in maximum wind speed, (2) enlargement of wind swath (Sitkowski et al. 2011), (3) increased storm surge generation (Irish et al. 2008), and (4) increases the area exposed to windborne risks, which would have major implications towards forecasts and public warnings.

In the work of Sitkowski et al. (2011), an eyewall is defined as a wind maximum, composed of three specific phases using aircraft-retrieved wind profiles: (1) *Intensification*, (2)

weakening, and (3) *reintensification*. In the *intensification* phase, both an inner (i.e., primary) and outer (i.e., secondary) eyewall intensify and undergo contraction with respect to storm radius. However, the intensification rate of the inner eyewall decreases throughout the *intensification* phase, while the outer eyewall continues to intensify. When the intensification of the primary eyewall stops, the *weakening* phase begins and proceeds until the intensity of the secondary eyewall exceeds the intensity of the primary eyewall. At this point, the ERC is in the *reintensification* phase and occurs until the primary eyewall is no longer detectable.

Kossin and Sitkowski (2009) have shown that cases of ERCs with no readily available aircraft data can be predicted with limited skill through environmental conditions and storm metrics such as (1) higher maximum potential intensities, (2) maximum wind speed, (3) weaker vertical wind shear, (4) weaker upper zonal-level winds, (5) a deep layer of warm water, (6) and higher middle- to upper-level relative humidity. These environmental conditions are also consistent with rapidly intensifying TCs (Merrill 1987; Lin et al. 2010; Kaplan and DeMaria 2003), hence, discerning if and when an ERC occurs can be challenging.

In addition to environmental conditions, ERCs can be observed using satellite passive microwave imagery, aircraft radar, and shore-based radar. 37 and 85–92 GHz passive microwave imagery has the ability to view the TC structure under the overlying canopy of high clouds (Hawkins and Helveston 2006), but cannot be captured by longwave infrared (IR) centered near 11 μm imagery or visible imagery. ERCs can also be captured by land-based radars, but the TC must be close to land and within range of the radar. Aircraft radar (NOAA WP-3D) also has the ability to capture the internal structure of TCs and ERCs, however, with the exception of the North Atlantic (ATL) and certain TCs in the Eastern North Pacific (WPAC), flight-based data for TCs are unavailable, resulting in an Atlantic-centric perspective of ERCs in most prior

studies. Hawkins and Helveston (2006) found that between the basins of the ATL, eastern North Pacific (EPAC), WPAC, and the Southern Hemisphere Ocean (SHEM), double eyewalls exists in about eight TCs yearly, with occurrence being the most frequent in the EPAC and the ATL basins, respectively. However, given the lesser availability of satellite imagery at the time, these values are likely an undercount.

A major gap in knowledge that needs to be addressed is the undercount of ERC occurrences globally. To understand TCs holistically, we must study ERCs over different basins, unfortunately, many ERCs occur undocumented without the availability of aircraft data. Fortunately, satellite data (passive microwave imagery) can be used to observe ERCs where aircraft data are unavailable. A caveat to using satellite data to document ERC climatology is that an objective and automated method is needed to ensure both consistency and efficiency. To document ERCs globally, this study creates a subjectively labeled dataset of TC secondary eyewalls and primary eyewalls constructed from passive microwave imagery from storms occurring in the ATL, EPAC, WPAC, and SHEM basins. In addition, using the labeled dataset, we design a first-of-a-kind secondary eyewall detection algorithm trained with relevant environmental conditions. Chapter 2 describes the consolidated dataset of TC passive microwave imagery and environmental variables that we used. Chapter 3 describes secondary eyewalls determination in our subjective labeled dataset, the predictors chosen, and the machine learning classifier. Chapter 4 discusses the verification metrics of our model and Chapter 5 summarizes the model and future work.

Chapter 2

Data

In this chapter, we will discuss the passive microwave imagery dataset, and environmental variables used in our subjective labeled dataset and detection algorithm, including details about how the data were processed. First, to create a labeled dataset of tropical cyclone secondary eyewall events and a secondary eyewall detection algorithm, we used the Tropical Cyclone Precipitation, Infrared, Microwave, and Environmental Dataset (TC PRIMED), a consolidated dataset of TC passive microwave imagery and environmental variables (Razin et al. 2022). Second, our detection algorithm for the presence of secondary eyewalls will follow a similar outline to the Herndon et al. (2018) algorithm, which involves feeding the following data types into a machine learning classifier: (1) passive microwave imagery, (2) environmental data and storm maximum wind speed, and (3) subjectively determined labels of whether a secondary eyewall exists at the time of a satellite overpass. The predictors (1) and (2), are retrieved from TC PRIMED, while the secondary eyewall labels are created using the methods described below.

2.1 Passive Microwave Imagery

In this study, we use information from passive microwave imagery as predictors of our detection algorithm because frequencies between 85–92 GHz have the ability to view TC convective structure below the overlying canopy of cirrus clouds (Hawkins and Helveston 2006). The passive microwave imagery provided by the TC PRIMED dataset includes various frequencies between 85–92 GHz from 1998–2019. However, only imagers between 2016–2019 were used since the labeled secondary eyewall dataset only consisted of storms from these years.

In addition, only horizontal and vertical (H & V) polarization imagers were selected to allow the use of polarization-corrected temperature (PCT; Cecil and Chronis 2018). PCT reduces the impact of low emissivity surface features, punctuating TC internal structure features such as eyewalls. Table 1 is a list of all the imagers used and their frequencies.

Table 1. Microwave Imagers Used

Passive microwave imagers used from 2016–2019 with frequencies varying from 89.0 GHz–91.665 GHz.

Passive Microwave Imager	Polarization	Frequency (GHz)
GPM Mission Imager (GMI)	H & V	89.0
Special Sensor Microwave Imager Sounder (SSMIS)	H & V	91.665
Advanced Microwave Scanning Radiometer 2 (AMSR2)	H & V	89.0

In addition to the selection of passive microwave images, there are also two considerations regarding TC PRIMED: (1) centering of the grid on the TC center, an important aspect that will be explained in the discussion chapter, and (2) the polar grid. For imagery centers, the storm centers are based on the Automated Tropical Cyclone Forecast system database (ATCF; Sampson and Schrader 2000) best-track center. Unfortunately, a drawback to using these centers as a starting point is that they are based on low-level (near-surface) circulations estimated every 6-h, while the ice-scattering captured by passive microwave imagers are typically at the mid-levels. Often, the vortex can be slightly misaligned due to parallax error and shear, leading to a poorly-centered image (Asano 2008). Lastly, the 4 km in radius and 10 degrees in azimuth polar analyses of the passive microwave imagery brightness temperature observations are created using a variational analysis technique (Mueller et al. 2006), reducing resolution discrepancy between imagers and sounders. The variational analysis technique has

half-power filter wavelengths of 32 km in radius and 90° in azimuth. Each of the above details can affect the quality and thus interpretation of the polar gridded passive microwave imagery.

2.2 Storm Maximum Wind Speed and Environmental Data

Similar to the Kossin and Sitkowski (2009) model, we also used estimates of the storm's current maximum wind speed and environmental data to better assist the classifier in determining the presence of secondary eyewalls. Table 2 outlines the environmental variables and storm intensity variables that were obtained from the TC PRIMED dataset.

Table 2. Environmental Variables and Storm Intensity

Environmental variables and storm intensity obtained from the TC PRIMED dataset.

	Environmental Variables and Storm Intensity
1.	Current Maximum Wind Speed (kt)
2.	Radius of 5 kt Winds at 850 hPa (R5)
3.	IR Brightness temperature (TB)
4.	800–250 hPa Deep Layer Shear Magnitude (0–500 km)

The sources of the environmental dataset in TC PRIMED include ERA5 and ATCF (Razin 2022). The current maximum wind speed is obtained from ATCF post-season best track data. The maximum wind speed (intensity) is chosen as an initial predictor because Kossin and Sitkowski (2009) have shown that models using intensity produce some skill in identifying secondary eyewalls. The radius of 5 kt winds at 850 hPa (R5) is calculated from longwave infrared imagery— a scaling factor that represents the general size of a TC (Knaff et al. 2014). R5 was chosen because Sitkowski et al. 2011 showed that ERCs often result in an expanded wind field. IR brightness temperatures (IR TB) are obtained from geostationary satellites with

central wavelengths near 11 μm and are a measure of cloud top brightness temperature. IR TB was chosen because we observed a slight warming of TC cloud top temperatures before and during ERCs. The storm-centered 800–250 hPa deep layer shear magnitude within a 500 km circular area is calculated using the ECMWF fifth-generational atmospheric reanalysis product (ERA5; Hersbach et al. 2020) based on centering procedures discussed in Slocum et al. (2022). This is chosen as a predictor because the secondary eyewall identifier in Kossin and Sitkowski (2009) associated SEFs with weaker wind shear.

Chapter 3

Methods

3.1 Labeled Dataset

In this chapter, we will discuss our methods in creating a labeled dataset of secondary eyewalls. The labeled dataset is a subjective dataset created using our own definitions for a TC eyewall and secondary eyewall for storms in the ATL, EPAC, WPAC, and SHEM basins. These labels are fed into our detection algorithm and are created using passive microwave imagery from TC PRIMED. Due to the subjective nature of this dataset, an analyst's confidence level is also estimated for each label. From TC PRIMED, we use 85–92 GHz passive microwave PCT imagery because the minimum in the brightness temperature values denotes strong scattering signals in convection associated with ice concentration and size. We define an eyewall as a ring of minimum brightness temperature (ice scattering) around the TC center in an 85–92 GHz PCT microwave image, and a secondary eyewall as a region of minimum brightness temperature outside the eyewall that extends more than 180° azimuthally. However, the secondary eyewall definition is subjected to spiral rainband determination, which is a convective band that meets this definition but is not a secondary eyewall due to its non-concentric characteristic. Figure 1 (left) shows an example from Typhoon Maria on 10:25 UTC 7 July 2018 with a spiral rainband, which involves an outer minimum in PCT that meets the definition of a secondary eyewall, but is a cold ring that radially crosses more than 150 km. In contrast, Fig. 1 (right) is an example of concentric eyewalls from Typhoon Maria on 10:13 UTC 9 July 2018, which has an outer minimum in PCT that is completely separated from the inner minimum in PCT and does not

spiral inwards towards the storm center. Concentric eyewalls are mature secondary eyewalls that completely surround the primary (inner) eyewall and result in an analyst's confidence level > 3.

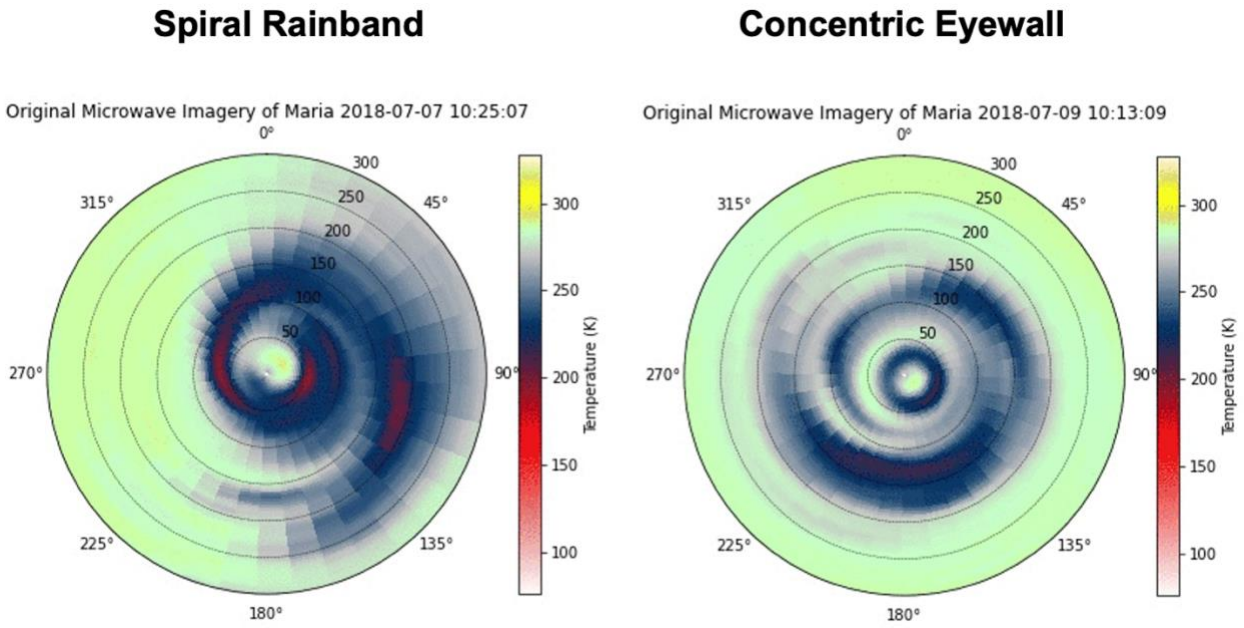

Figure 1. Spiral Rainband vs. Concentric Eyewall

An 89 GHz PCT microwave image depicting a spiral rainband (left) versus a concentric eyewall, a mature secondary eyewall (right) of Typhoon Maria (2018) at Typhoon Maria on 10:25 UTC 7 July 2018 and 10:13 UTC 9 July 2018, respectively. Red colors represent lower temperatures [K] and yellow colors represent higher temperatures [K]. The convective bands in the TC internal structure are represented by the blue and red colors due to ice scattering.

For analyst's confidences levels, values from 1 to 5 were assigned to each label, from least confidence to most confidence. These confidences applied to both 'yes' and 'no' labels for the presence of a primary (inner) eyewall and of a *secondary eyewall*. For example, if a secondary eyewall label is 'yes,' the confidence level indicates how confident the analysts are that a secondary eyewall is present. However, if the secondary eyewall label is 'no,' then the confidence level represents the confidence that a secondary eyewall is *not* present. Confidence labels allow for more thorough interpretation of model performance as will be discussed in Chapter 4.

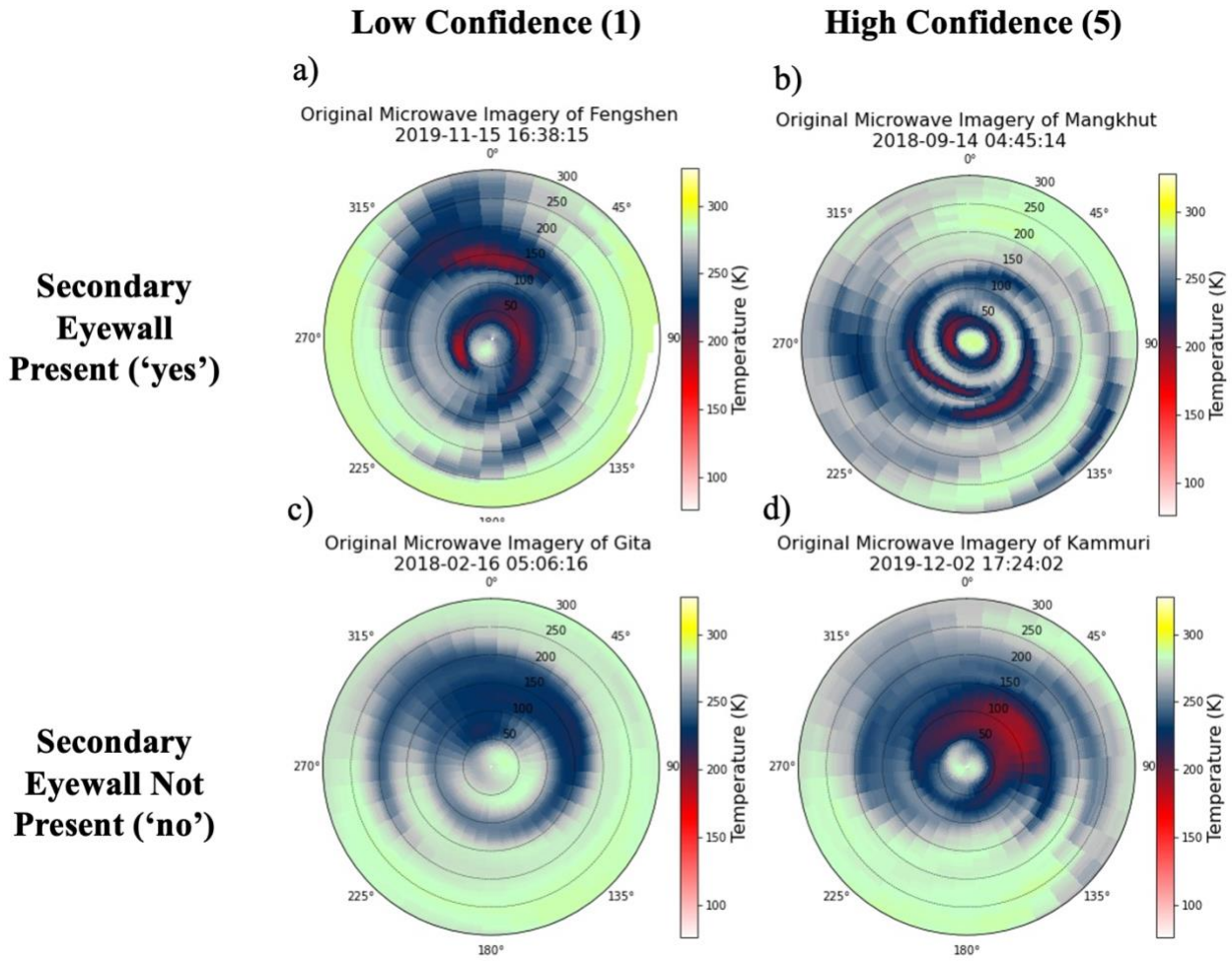

Figure 2. Secondary Eyewall Labeling and Confidences

Same image type as in Figure 1. Cases of high (5) and low (1) confidences associated with both 'yes' and 'no labels for creating the labeled dataset. (a) Involves a low confidence 'yes' label. (b) Involves a high confidence 'yes' label. (c) Involves a low confidence 'no' label. (d) Involves a high confidence 'no' label.

In Fig. 2a, a 'yes' label for secondary eyewall was assigned because there appears to be a pronounced moat between an outer and inner minimum, however, there is low confidence in this label due to the spiraling nature of the outer minimum and a slight connection between the two minima at 225°. For Fig. 2b, an outer concentric minimum with a prominent presence of a moat between the two minima resulted in a high confidence 'yes' label. For Fig. 2c, a 'no' label for secondary eyewall was assigned because an outer minimum spirals inwards towards the inner

minimum, with a more ambiguous moat between the two minima than in the low confidence ‘yes’ label. However, a moat is present at 225°–315° with the outer minimum showing a segment of concentricity with the primary (inner) eyewall, hence, this label was low confidence. Lastly, for Fig. 2d, a prominent inner minimum is present, with no prominent outer minimum features, hence a high confidence ‘yes’ label for secondary eyewall was assigned. The results of the labeled dataset will be discussed more in detail in Chapter 3.3.

3.2 Generating Microwave Image Variables (predictors)

Now that we have discussed the sources of data for the three parts of our detection algorithm: (1) microwave imagery, (2) environmental and storm maximum wind speed, and (3) secondary eyewall labeled dataset, we will now detail how the first two datasets were used to generate predictors. The microwave image variables involved many detailed steps, beginning with filtering the image using a Gaussian filter (Appendix A; Virtanen et al. 2020). After generating the filter, we found the difference between the PCT image and the filter and denoted this as the signal image. The parameters chosen in the filter were fine-tuned to allow this signal image to depict the features of the internal structure of the TC convective bands and moats as negative and positive signals, respectively. Next, we also normalized all the images to fractional R5 (fR5), which is the satellite R5 (see Chapter 2.2) value divided by the climatological R5 value as a function of intensity (Knaff et al. 2017). This normalization allows us to compare the locations of internal TC features of storms of varying sizes since large storms can have convective bands at a greater radius than smaller storms (Knaff et al. 2014). While fR5 normalizes the storm radii, we also normalized storm motions, since we observed in microwave

imagery that rainbands typically wrap around the storms relative to the storm motion. To do this, we rotated all the microwave imagery using the best-track storm direction. Figure 3 depicts the motion of a typical convective band after the storm-relative motion adjustment.

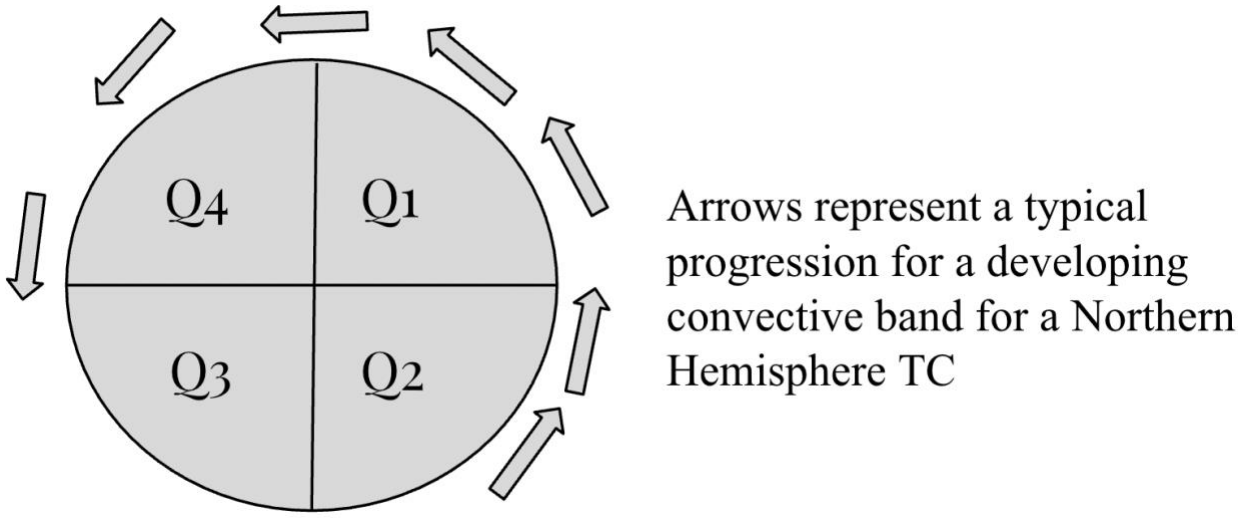

Figure 3. Convective Band Progression

A typical progression of a convective band in a Northern Hemisphere TC. This diagram depicts the flow in a storm-relative framework. Typical convective bands develop in Q2, then begin to wrap around the remaining quadrants cyclonically (Counter-clockwise in the Northern Hemisphere and clockwise in the Southern Hemisphere).

After adjusting for the size and direction of motion, we divided the TC into 16 equal azimuthal sectors and calculated the radial signal means for each sector. Several different quantities of sectors were tested, however, we determined that using more sectors was better because it provided greater spatial resolution of the image. Fewer sectors resulted in larger azimuths, hence, small-scale details are more likely to be missed. Unfortunately, a disadvantage to using more sectors is the potential for more noise in the data. To mitigate this, each sector mean was weighted using two neighboring sector means (25% for each neighboring sector and 50% for the sector being evaluated). We defined these data as the ‘shared’ signal mean. Next, we located the minima in each of the ‘shared’ signal mean curves using a fourth order argument

relative extrema method for identifying peaks in signals (using SciPy). A rolling window of 4 data points (16 km radius) on each side of the curve was considered for finding each minimum. However, the minima found from this tool were generally generally noisy and sometimes included points that did not represent convective bands. To filter out features that were unlikely to be associated with secondary eyewalls, we only accounted for minima that had a signal < -8 K, which indicates deep vigorous convection, and within a 300 km radius, a conservative outer limit for a secondary eyewall. This –8 K threshold was determined subjectively after examining many thresholds ranging from –4 K to –15 K and the resulting minima counts vs. the features seen in the corresponding 2D image. With the locations of the minima as a function of storm radius, we now have derived useful information regarding where potential convective bands are located.

In order to interpret the minima locations, we used a windowing technique that counts the number of minima in 8−64 km (interval of 4 km) radius windows and averaged all windows. This range of windows was chosen because the smaller windows can detect finer small-scale details (more noise), while the larger windows can detect smoother large-scale details (less noise). The average of all the windows in this range reduces noise while also allowing the small-scale details to still be detected. The result of this windowing technique is a single curve that represents the number of minima with respect to storm radius (Fig. 4). The top row in Fig. 4 shows a concentric eyewall case for Typhoon Maria on 10:13 UTC 9 July 2018 where the peaks for each eyewall are located at 30 and 135 km, respectively. The bottom row in Fig. 5 shows a spiral rainband case for Typhoon Maria on 15:55 UTC 6 July 2018 where a single peak represents a single eyewall at 60 km. Note that in the spiral rainband case, the curve decreases much more gradually than the concentric eyewall case.

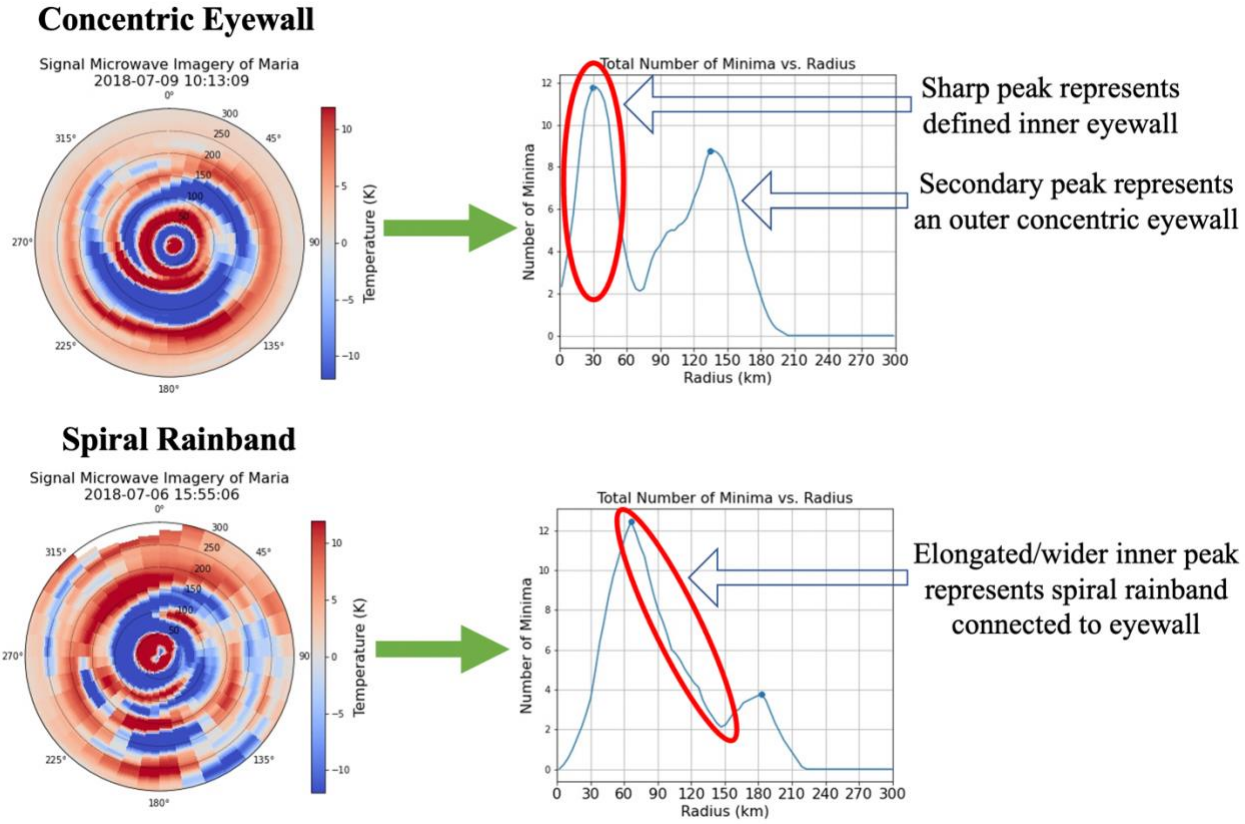

Figure 4. Signal Microwave Imagery and Resulting Total Number of Minima Plot

Resulting total number of minima curves (after windowing technique) as a function of TC radius from microwave signal images of Typhoon Maria (2018). The top row (concentric eyewall present) curve indicates two peaks (blue scatter points) that represent an inner and an outer eyewall. The bottom row (spiral rainband present) curve depicts only one peak and an elongated inner peak descent beyond 70 km radius.

In addition to the curves in Fig. 4, the detected peaks (blue scatter points) are very important because they provide information regarding the location(s) of potential inner and outer eyewall(s). These peaks are found by detecting the following characteristics of each maximum in the curve: (1) height of the peak, (2) minimum distance between maxima, (3) prominence of each maximum peak, and (4) width of each maximum peak (Appendix B). The height parameter removes peaks that do not encompass enough storm sectors and the distance parameter ensures that the same peak does not result in two detected peaks. The prominence parameter requires that only peaks that are distinguished from the rest of the curve are chosen. Lastly, the width

parameter requires that the peak (or convective band) must span across at least a 3-km radius. The resulting plot is a curve that typically has multiple peaks in the presence of multiple eyewalls and a single peak for a single eyewall.

With the information from the total number of minima curve and its detected peaks, image variables can now be extracted as predictors. The three image variables that we chose in this study include: (1) the number of minima peaks, (2) the magnitude of the second peak, and (3) the distance between the first and second peaks. Image variable (1) is the total number of peaks detected by our peak detector. Image variable (2) is the number of minima of the second-innermost peak, given that there is an inner peak as well. Image variable (3) is the radial distance in km between the innermost and second-innermost peaks. If less than two peaks are detected, then image variables (2) and (3) are equal to zero. Based on observations of the curve plots from various storms, we found that, (1), a greater number of minima peaks, (2), a larger magnitude of the second peak, and (3), a smaller distance between the first and second peak are associated with the presence of secondary eyewalls. We will further discuss the choice of these variables with their associated coefficient values in the results chapter.

3.3 Generating Environmental and Storm Metrics Variables (Predictors)

In addition to image variables derived from the passive microwave imagery, we will discuss in this chapter section how we incorporated environmental and storm metrics variables outlined in Table 3 as predictors. First, the current maximum wind speeds were obtained directly from the TC PRIMED because the times were already linearly interpolated to each passive microwave image time. For the remaining variables, a cubic univariate spline was fitted (using

SciPy) to model the temporal evolution of each variable, allowing us to produce values at the time of each available microwave image. Our hypothesis for the variables R5 and IR TB was that the 24-hour differences (wind field expansion/contraction and cloud top temperature changes) were more associated with secondary eyewalls than single-time values, hence, 24-h differences were applied to the existing splines (also in a cubic spline). In terms of wind shear, we hypothesized that ERCs generally occur at lower magnitudes (<8 ms^{-1}), hence, no differencing was needed. To substantiate these relationships, we compared Tables 4 and 5. Table 4 details the number of cases within each confidence level, the standard deviation, and the average for all variables (current maximum wind speed, 24-h Difference in Radius of 5 kt Winds at 850 hPa, 24-h Difference in IR Brightness temperature, and 800–250 hPa Deep Layer Shear Magnitude) for all 'yes' secondary eyewall (SE) labels. Table 5 is the same as Table 4, but for all 'no' SE labels.

Table 3. Environmental Variables and Storm Intensity Predictors

Environmental variables and storm intensity predictors.

	Environmental Variables and Storm Intensity Predictors
1.	Current Maximum Wind Speed (V_{max})
2.	24-h Difference in Radius of 5 kt Winds at 850 hPa (24-h R5)
3.	24-h Difference in IR Brightness temperature (24-h IR TB)
4.	800–250 hPa Deep Layer Shear Magnitude (Shear)

Table 4. Labeled Dataset Statistics ('yes' labels)

Storm intensity and environmental variables of SE 'yes' labels (>33 m s^{-1}) by confidence levels. Average and standard deviations were calculated for V_{max}, shear, 24-h difference in IR TB, and 24-h difference in R5 at each confidence level. The cases represent the number of 'yes' labels at each confidence level.

Conf.	Cases	Avg V_{max} (m s^{-1})	Std V_{max} (m s^{-1})	Avg Shear (m s^{-1})	Std Shear (m s^{-1})	Avg 24-h IR TB (K)	Std 24-h IR TB (K)	Avg 24-h R5 (km)	Std 24-h R5 (km)
1	40	55	11	4.90	2.92	6.68	12.64	158.02	414.46
2	88	51	11	5.34	2.27	2.67	15.34	176.31	578.28
3	67	55	10	5.69	2.76	0.62	13.07	144.84	742.04
4	61	58	10	5.10	2.94	6.41	11.61	93.77	415.02
5	34	62	11	5.49	2.14	6.61	10.23	20.17	141.19

Using the information regarding V_{max} in Tables 4 and 5, we found that the average V_{max} in the 'yes' labels were significantly larger than the 'no' case, especially in the higher confidence cases (4 and 5) and is consistent with our hypothesis to use V_{max} as a predictor. Note that only labels >33 m s^{-1} were considered in both Tables 4 and 5. Next, we observe that the average wind shear of varying confidences for the 'yes' labels was in the range of 4.90−5.69 m s^{-1}, while the 'no' labels ranged from 6.00−9.68 m s^{-1}. For the average 24-h IR TB, we found that the different confidence 'yes' labels ranged from 0.62−6.68 K, while the 'no' labels ranged from 2.22−25.69 K. Lastly, for the average 24-h R5, the different confidence 'yes' labels varied from 20.17−176.31 km, while the 'no' labels ranged from −70.00−33.87 km. In summary, the 'yes' and 'no' labels produce clearly distinguishable differences of average values for the chosen variables at varying confidence labels, hence, we expect favorable incorporation of these variables into a machine learning classifier.

Table 5. Labeled Dataset Statistics ('no' labels)

Same as Table 4 but for 'no' labels.

Conf.	Cases	Avg V_{max} (m s^{-1})	Std V_{max} (m s^{-1})	Avg Shear (m s^{-1})	Std Shear (m s^{-1})	Avg 24-h IR TB (K)	Std 24-h IR TB(K)	Avg 24-h R5 (km)	Std 24-h R5 (km)
1	19	49	10	7.83	6.10	18.18	29.82	–62.92	321.38
2	78	52	10	6.54	4.10	6.10	13.46	–63.01	498.98
3	148	52	10	6.00	3.75	2.22	21.28	33.87	507.36
4	163	48	10	6.63	4.50	10.10	23.38	–70.00	376.84
5	183	43	9	9.68	6.07	25.69	46.91	–30.56	1113.03

3.4 Machine Learning (Classifier)

The machine learning classifier that we used is a linear discriminant analysis (LDA) since we generally visualized the correlation between each of the predictors with the existence of secondary eyewalls as a linear relationship (Virtanen et al. 2020). In terms of providing the predictors, all values provided were based on times of available passive microwave imagery. Thirty-six storms from various basins were used to fit (train) the classifier and 16 storms were used for testing. Appendix C lists the storms used for each dataset. An additional independent validation dataset of 18 storms also exists, but those results will be discussed in future work. In total, 70 storms were randomly distributed by basin and season from the labeled dataset among the training, testing, and validation datasets. Lastly, these analyses were only applied to storms with maximum wind speeds > 33 m s^{-1}, or as or more intense than a category 1 hurricane according to the Saffir-Simpson Wind Scale.

Chapter 4

Results

In this chapter, we will detail the results of our secondary eyewall detection algorithm using various validation metrics. First, in our LDA classification, the probability of a secondary eyewall presence (*P*) in % is calculated at the time of every available passive microwave image. The model is fitted from the 36 storms in the training dataset and tested on the 16 storms in the testing dataset. The standardized correlation coefficients associated with our model fitted using the training dataset are given in Table 6.

Table 6. Standardized Coefficients for Fitted Model

Standardized correlation coefficients for each of the variables (predictors) in the model fitted with the training dataset. Generally, a larger coefficient value would indicate greater importance in the classifier.

Variable (Predictor)	Coefficient
Number of Minima Peaks	2.1×10^{-1}
Second Peak Magnitude	1.45×10^{0}
Distance between Peaks 1 and 2 (km)	-5.7×10^{-3}
24-h Difference in Infrared Brightness Temperature (K)	-3.6×10^{-3}
24-h Difference in Radius of 5 kt Winds (R5) (km)	2.1×10^{-1}
Current Maximum Wind Speed (kt)	6.9×10^{-1}
800–250 hPa Deep Layer Shear Magnitude (ms^{-1})	-1.1×10^{-1}

In Table 6, we observe that the largest correlation coefficient value in our model is the second peak magnitude, which indicates that the model heavily relies on this imagery-based variable. A positive value is expected because a greater second peak magnitude is associated with an outer convective band that encompasses more azimuthal sectors at a smaller range of

storm radii. The next most important variable is the current maximum wind speed, which has a correlation coefficient because intense TCs (>96 kt) are much more likely to form secondary eyewalls (Hawkins and Helveston 2006; Kossin and Sitkowski 2009), while storms weaker than 70 kt are often disorganized and lack a clear primary eyewall. Note that we use the 6-hourly best-track intensity, and this does not capture storm intensity fluctuations that are associated with quick ERCs that occur on timescales less than 6-h. Thirdly, the 24-h difference in R5 and the number of minima peaks are similar in terms of importance and are both positive values. These variables are also consistent with our hypothesis since a TCs wind field is expected to expand during the ERC process. In terms of the number of minima peaks, it may seem counterintuitive that the number of minima peaks can exceed 2 or 3 peaks (double or triple eyewalls), as this variable is intended to detect the number of eyewalls, the algorithm is imperfect and can misinterpret pixelated microwave images and spiral rainbands as peaks. As a result, more minima peaks correlate with a greater probability that a detected peak is a secondary eyewall. The remaining three variables (800–250 hPa Deep Layer Shear Magnitude, 24-h Difference in Infrared Brightness Temperature, and Distance between Peaks 1 and 2 have negative correlation values and are also consistent with our hypotheses. Consistent with our correlation coefficient for shear, Kossin and Sitkowski (2009) also found that ERCs are more likely to occur in low-shear environments. In terms of the 24-h difference in IR brightness temperatures, we also expected that cloud top temperatures typically cool during ERCs during the reintensification phase. Lastly, the correlation value for the distance between peaks 1 and 2 in the microwave imagery is also negative. Theoretically, peaks 1 and 2 are our innermost and second-innermost eyewalls, however as discussed before, spiral rainbands and pixelated images are sometimes misinterpreted as peaks. As a result, we expect the distance between peaks 1 and 2 to decrease as the secondary

eyewall intensifies and contracts due to angular momentum conservation. In summary, the correlation coefficients associated with each variable were consistent with our expected likelihood of secondary eyewall formations.

Next, we will present the accuracy of the testing dataset using four metrics: (1) probability of detection (POD), (2) false alarm ratio (FAR), (3) critical success index (CSI), (4) Peirce's skill score (PSS), and (5) bias ratio. Note that the default assumption in our model for 'true' label and 'false labels are when $P \geq 50\%$ and $P < 50\%$, respectively. We define POD as the ratio of hits (true positive) and the sum of hits and misses (false negatives). In contrast, the FAR is the ratio of the number of false alarms (false positives) and the sum of false alarms and hits. Ideally, a high POD and a low FAR would indicate that a model has good skill in detecting an event without many false alarms. Next, CSI, also known as the threat score, is the ratio of hits and the sum of hits, misses, and false alarms. CSI tells us about the performance of the model with respect to both false alarms and hits. PSS tells us how well 'true' and 'false' labels are separated by our model (Roebber 2009). Lastly, the bias ratio measures how well the forecasted 'yes' events compare to the observed frequency of 'yes' events. Table 7 details the results of our model using these metrics.

Table 7. Model Results of Testing Dataset (50% Threshold)

Results of our model (testing dataset) using a default P threshold of 50% for a true label. A higher POD indicates the model's ability in detecting secondary eyewalls events (true positives) and a lower FAR indicates the model's skill at reducing false alarms (false positives). The CSI and PSS indicate a model's ability based on the combination of POD and FAR and ranges from 0 (no skill) to 1 (perfect). The bias ratio represents the tendency of this model's forecasts.

Assumption	Probability of Event Detection (POD)	False Alarm Ratio (FAR)	Critical Success Index (CSI)	Peirce's Skill Score (PSS)	Bias Ratio
Default (50% threshold)	0.64	0.34	0.48	0.52	0.98

Table 7 indicates that the model has some moderate skill (POD > 0.50 and FAR < 0.35) in detecting secondary eyewall events while limiting the number of false alarms using a P = 50% threshold. In addition, CSI and PSS scores, which range from 0 (no skill) to 1 (perfect), also indicate that the model was moderately skillful (≈0.50). We can also evaluate whether the model skill was consistent with the confidence levels of our labels by plotting bar charts of each of the four possible outcomes (true positive, true negative, false positive, and false negative) with respect to various label confidences (Figs. 5a–d). For Fig. 5a, we found that there was a lower frequency of true positives for label confidence of 1 and the greatest frequency being a confidence level of 3. Note that in our labeling, the confidences were not evenly distributed and the requirement to be categorized as a confidence level of 5 was a very well-defined concentric eyewall, hence label frequencies of 2–4 were much more common than 5 (Table 4). In Fig. 5b, true negative forecasts for a confidence level of 5 were the most common, followed by a sequential decrease to 1. In Fig. 5c, a confidence level of 3 was the most common for a false positive forecast followed by a confidence level of 2. However, these two levels had the highest frequencies by far, 12 and 9, respectively, while the third-highest frequency was only 3. Lastly, for Fig. 5d, the confidence level of 2 had the greatest frequency for the false-negative label,

followed by a confidence level of 1. Ideally, the true positive and negative labels should have the greatest frequencies at the highest confidence levels and the false positive and negative labels should have the greatest frequencies at the lowest confidence levels, which is reflected only in the true negative bar plot (Fig. 5b). The other bar plots generally show this but do not have a persistent trend.

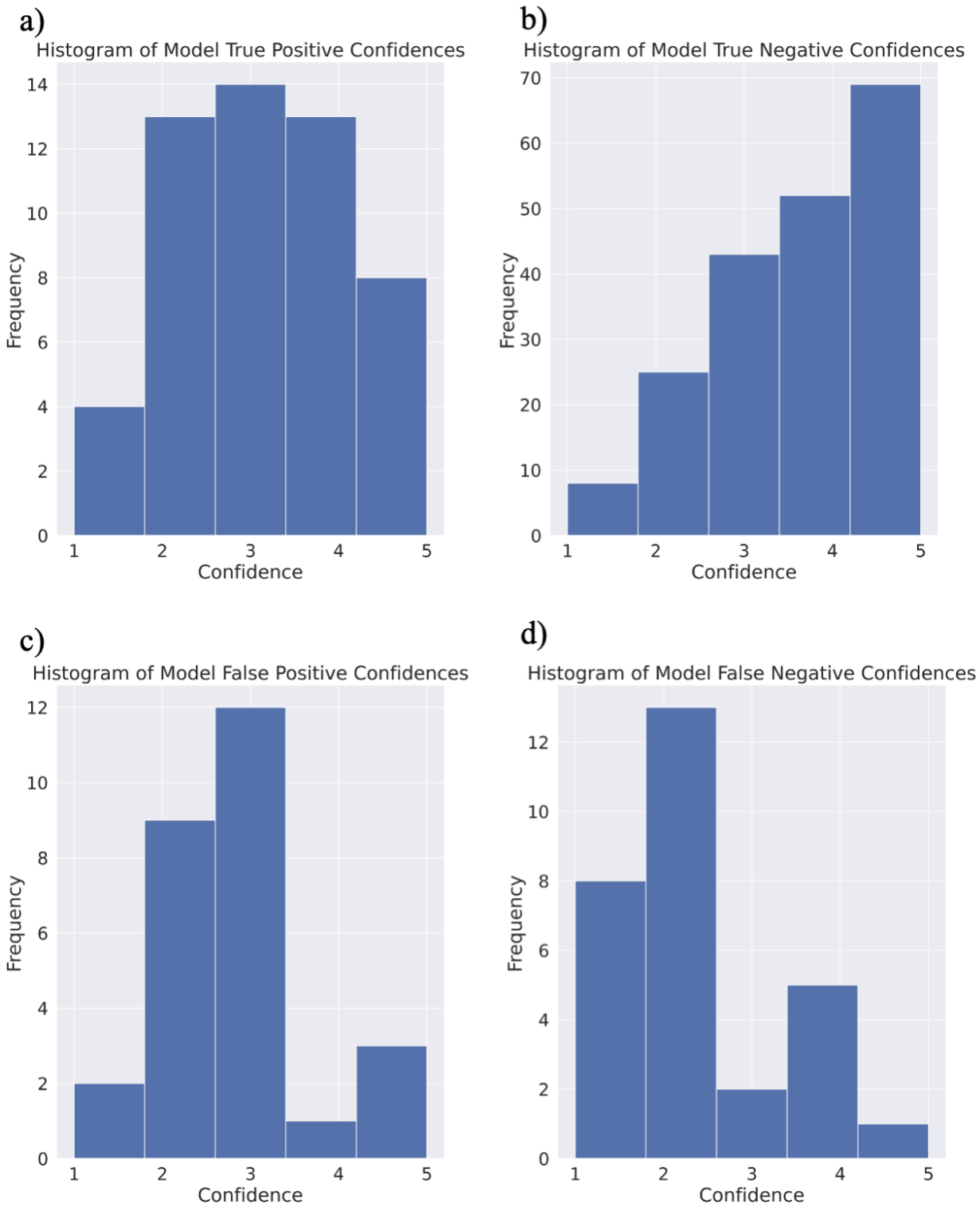

Figure 5. Histograms of Model Verification by Label Confidence

Histogram of label confidences with respect to model (a) true positives, (b) true negatives, (c) false positives, and (d) false negatives.

The data in Fig. 5 were not normalized and do not portray an accurate depiction of the confidence with respect to our model. Figure 6 bins *P* into intervals of 14.29% and calculates the mean label confidence level for each respective bin. We expect a minimum in the mean confidence label where the model *P* approaches 50% since this would indicate consistency between low confidence labels and low model confidence. In Fig. 6, we observed that the highest mean label confidence level is located at the lowest *P* bin and the third-highest mean label confidence is at the highest *P* bin. In contrast, the lowest mean label confidence level is binned in $29\% < P < 43\%$. The mean label confidences levels between all the *P* bins only varied moderately, from 2.67–3.76, which indicates that the model experienced similar difficulties with labeling as the human-created labels, but also has some room for improvement. In summary, a larger range would indicate better consistency between the two labels, since a low confidence label should also result in a lower *P*.

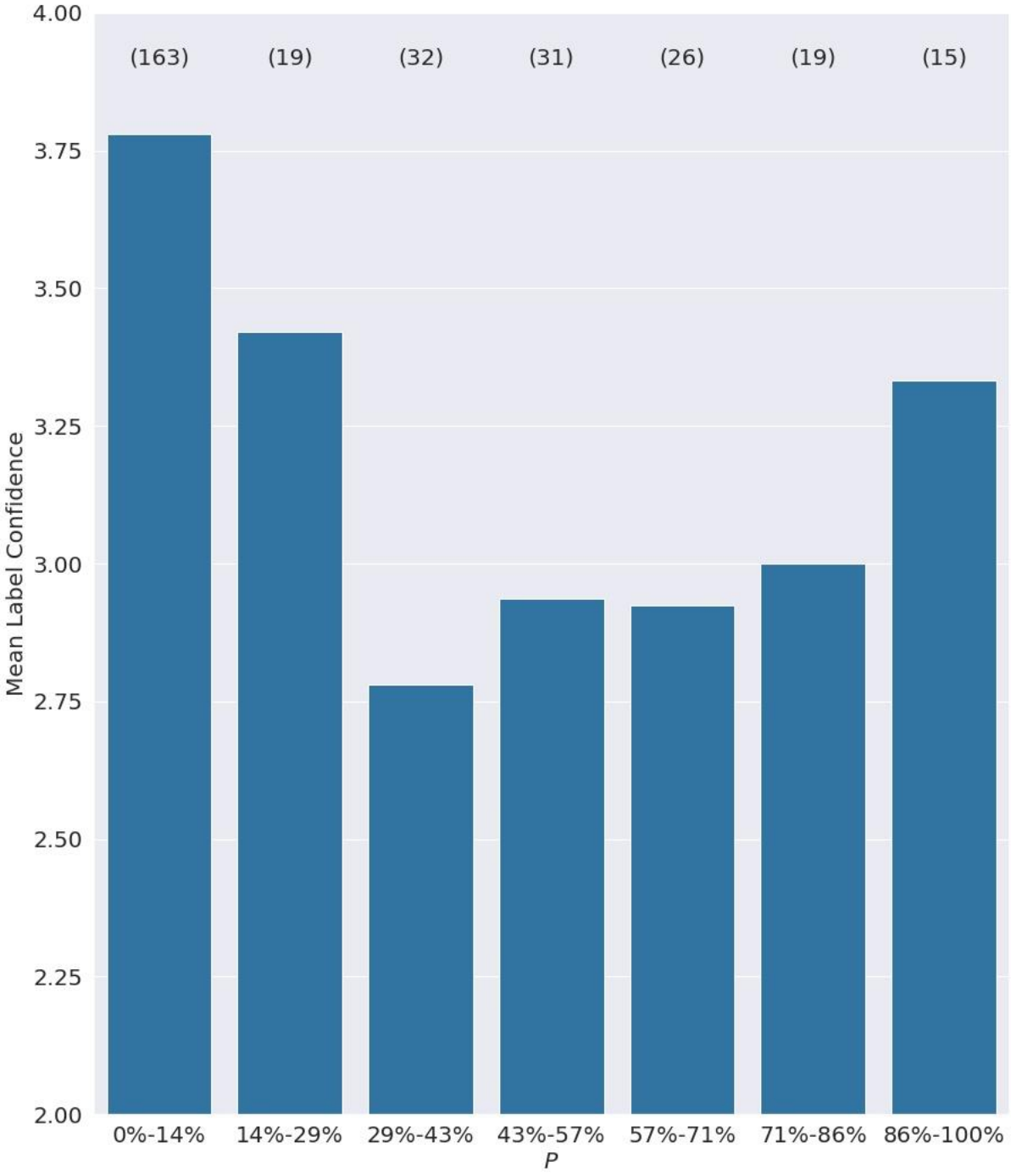

Figure 6. Bar Plot of Mean Label Confidence and Model Probability

Bar plot of mean label confidences for various bins of P (testing dataset). The value inside the parenthesis above each bar represents the sample size of each bin.

In addition to using a default *P* threshold that we discussed earlier, we can also optimize the scores in Table 7 by choosing a *P* that maximizes the threat score (CSI) or a bias ratio closest to 1 (Wilks 2019). Figure 7 represents the bias ratio and threat score as a function of *P* for the testing dataset. We found that while the threat score was generally flat, the maximum was located at *P* = 28%. Table 8 details the verification scores using this threshold.

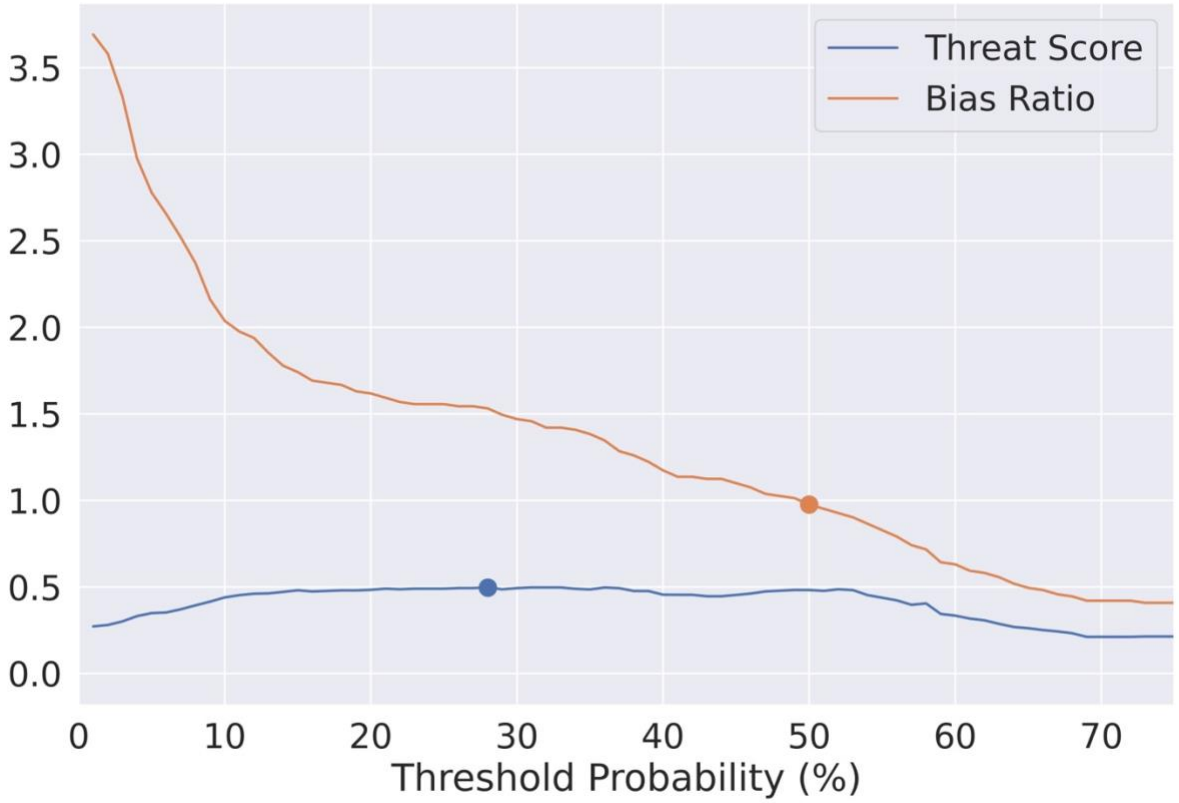

Figure 7. Threat Score and Bias Ratio as a Function of Threshold Probability

Threat score (blue line) and bias score (orange line) as a function of varying P thresholds for the testing dataset. The blue point represents the threshold P that generates the maximum threat score. The orange point represents the threshold P that results in a bias ratio nearest 1.

Table 8. Model Results of Testing Dataset (Threat Score Optimized Threshold)

Same as Table 7 but using a threshold that maximizes the threat score (CSI).

Assumption	Probability of Event Detection (POD)	False Alarm Ratio (FAR)	Critical Success Index (CSI)	Peirce's Skill Score (PSS)	Bias Ratio
Threat Score Assumption (28% threshold)	0.84	0.46	0.49	0.73	1.53

We observe in Table 8 that while the threat score is maximized, the CSI is only 0.01 higher than the default assumption (Table 7). However, the POD increases dramatically from 0.64 (default assumption) to 0.84, while the FAR increases modestly from 0.34 (default assumption) to 0.46. In addition, the PSS also increases from 0.52 to 0.73, which indicates that the model does a better job of separating true and false labels. While these results show a significant improvement, the bias ratio is also much higher (0.98 → 1.53) in favor of a 'yes' label. Hence, another method that we can optimize our scores is using a threshold that results in the least bias (bias ratio → 1). Table 9 represents this assumption.

Table 9. Model Results of Testing Dataset (Bias Ratio Optimized Threshold)

Same as Tables 7 and 8, but using a threshold based on where the bias ratio is nearest to 1.

Assumption	Probability of Event Detection (POD)	False Alarm Ratio (FAR)	Critical Success Index (CSI)	Peirce's Success Score (PSS)	Bias Ratio
Threat Score Assumption (49% threshold)	0.65	0.35	0.48	0.51	1.01

The most notable observation in Table 9 is that the bias ratio-based threshold (49%) is very near our default assumption of 50%. This is not surprising because the default assumption

already had a bias ratio very near 1 (0.97). As a result, the POD and FAR only increased by 0.01 and the CSI remained the same from the default assumption. The PSS decreased by only 0.01 as well. In summary, both the threat score and default assumptions for the *P* threshold provide similar POD, FAR, and CSI values with minimal model bias.

Next, we will discuss a false alarm case to address potential contributors to the FAR. Figure 8 is an example from Tropical Cyclone Gita on 03:52 UTC February 14, 2018. A primary eyewall with a spiral rainband is depicted by a signal microwave image in Fig. 8a with the resulting plot of total number minima and detected peaks in Fig. 8b. We observe in Fig. 8b that two separate peaks are depicted, indicative of a double eyewall. However, our labeled dataset determined that there is only one eyewall and a spiral rainband, so we would have expected a gradual decline similar to a spiral rainband demonstrated in Fig. 4, rather than two peaks. In Fig. 8a, we see that the center of the inner eyewall from the ice scattering is displaced towards 45°. An ill-centered storm is problematic because our algorithm takes the azimuthal average of 16 storm sectors and creates a minima plot as a function of storm radius, hence, our model would distribute the same eyewall over a wide range of radii.

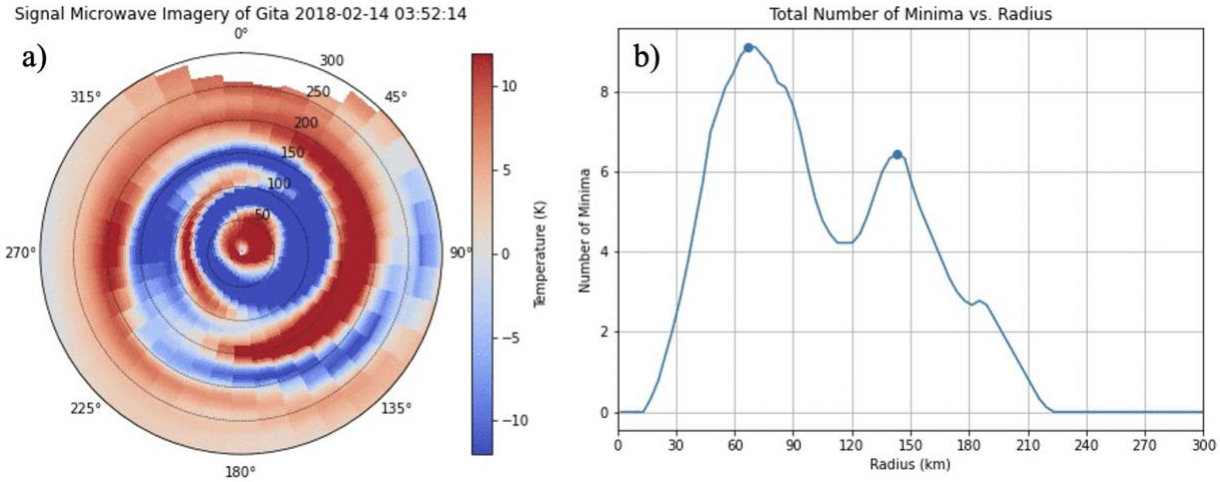

Figure 8. A False Alarm Case (Bad centering)

A false alarm case: (a) A primary eyewall and spiral rainband of Tropical Cyclone Gita on 03:52 UTC February 14, 2018, depicted by a signal microwave image. (b) The resulting total number of minima plot (blue curve) and the detected peaks (blue scatter points).

Chapter 5

Discussion and Conclusion

In this study, we designed a secondary eyewall detection algorithm using satellite passive microwave imagery, IR imagery, storm metrics, and environmental conditions. This is the first secondary eyewall detection algorithm that is trained using labels from multiple basins (refer to Chapter 3.1). One of the earliest methods of a secondary eyewall detection algorithm is described in Kossin and Sitkowski (2009). Their method used environmental and geostationary satellite features to detect secondary eyewalls. Without the same availability of passive microwave imagery at the time, their model produced less robust PODs (0.30) and PSSs (0.28) than our model (Tables 7–9), which includes information from the 89–92 GHz microwave imagery. A related effort was a forecasting algorithm known as the Microwave Probability of Eyewall Replacement (M-PERC; Kossin and DeMaria 2016) model. M-PERC uses information from 85–92 GHz microwave imagery, however, this model is only trained using storms from the ATL basin and is trained to forecast the timing of ERCs. In addition, M-PERC is more forecasting-centric and its POD is measured as the completion of an ERC within 24-h of an ERC (Wimmers 2018) onset according to the phases outlined in Sitkowski et al. (2011), which our labeled dataset found as too idealized. In other words, we found that when secondary eyewalls form, they do not always complete or abide by the exact evolution of *intensification*, *weakening*, and *reintensification*. In addition, some ERCs can occur so quickly (<12-h), that very few or no image of the process is captured by passive microwave imagery. In fact, the labeled dataset discussed in Chapter 3.1, which uses passive microwave imagery, found that at least 12.8% of named storms in 2016, 12.6% of named storms in 2017, 24.3% of named storms in 2018, and 19.6% of named storms in 2019 had at least one secondary eyewall, which is much more

frequent than found in Hawkins and Helveston (2006) when passive microwave imagery availability was more limited. Hence, our model is designed to determine the existence of a secondary eyewall at the time of an available passive microwave image. Overall, we found our model was able to detect (CSI = 0.48) and discriminate secondary eyewalls (PSS = 0.52) with relatively few false alarm events and low bias. This model's ability enables discrimination of candidate secondary eyewalls in the TC PRIMED dataset, creating a climatological dataset of ERCs globally. Such a global dataset would be instrumental in future research of ERCs and will expand our understanding of the dynamics of this process beyond the ATL basin.

Although the results of this model are promising, there are three aspects that still need to be improved in future work: (1) detection algorithm, (2) labeled dataset, and (3) machine learning methods. In terms of the detection algorithm, we found in Fig. 8 that our model is vulnerable to false alarms in storms with long spiraling rainbands due to the poor centering of some passive microwave images. Better-centering accounting may drastically improve our predictors by producing more consistent total number of minima plots. Another area of improvement that is needed in the detection algorithm involves the use of environmental variables. An example of such is the 24-h IR TB in the labeled dataset statistics (Tables 4 and 5). Both the ‘yes’ and ‘no’ labels indicated cloud top warming, but the ‘no’ labels warmed significantly less than the ‘yes’ labels, which indicates that the ‘no’ labels only warmed significantly because they were likely in the presence of an environment that was unfavorable for future TC development. Such findings suggest that this variable lacks importance (low correlation coefficient value in Table 6) and may need to be used differently. Lastly, a sensitivity analysis for the Gaussian filter and find peak functions (detailed in Appendices A and B) need to be performed to optimize the performance of the model.

The next aspect of future work includes expanding the labeled dataset to include more seasons and cases located in the North Indian Ocean basin. This is important to reduce confirmation bias and inconsistent techniques during the labeling process. The last aspect of future work is to test machine learning methods other than LDA, such as a quadratic discriminant analysis (QDA) or a random forest classification. For example, we suspect that the relationship between the number of minima peaks (predictor), and the predictand is likely to lie somewhere between linear and quadratic, since sometimes disorganized TCs feature many convective bands, causing many detected peaks, while, organized TCs often only have one or two detected peaks. This research has already begun and will be continued through the support of the NOAA Lapenta Internship.

Appendix A

SciPy Functions Parameters

Table A1 represents the parameters used in the gaussian_filter function in SciPy. The standard deviations for the azimuth axis (1) and radial axis (13) for the Gaussian kernel are adjusted and chosen to create signals in passive microwave images that would emphasize eyewalls and convective bands. The modes, azimuth, and radial, provide the function information on how to account for an overlapping border with the filter. Table A2 represents the parameters used in the find_peak function in SciPy. This function is used to determine peaks in the total number of minima plots (see Chapter 3.2). The minimum peak height (3.5) was determined qualitatively and adjusted until most detected peaks represent eyewalls. The minimum peak separation (10 km) is also adjusted to filter out any individual peaks that may be falsely determined as two peaks. The minimum peak prominence (km) was adjusted until most secondary eyewalls were detected as peaks. Lastly, the minimum peak width (km) is also adjusted to represent an eyewall that is at least 3 km wide, a very conservative standard.

Table A1. Parameters used for the Gaussian filter in SciPy.

Function	Standard Deviation for Azimuth Axis	Standard Deviation for Radial Axis	Mode (azimuth)	Mode (radial)
gaussian_filter	1	13	'wrap'	'reflect'

Table A2. Parameters used for the function to find peaks in the total number of minima plot in SciPy.

Function	Minimum Peak Height (Windowed Number of Minima)	Minimum Peaks Separation (km)	Minimum Peak Prominence (Windowed Number of Minima)	Minimum Peak Width (km)
find_peak	3.5	10	1.01	3

Appendix B

Storms in Labeled Dataset

Table B represents the TC distributions in the training, testing, and independent validation dataset. 36, 16, and 18 storms were randomly selected for training, testing, and independent validation datasets, respectively. The random selection was performed by first sorting all the labeled dataset storms by year and basin. Next, storms were randomly selected for each dataset, while maintaining an approximate ratio between the datasets of 2:1:1 by both year and basin. The storms below are listed using ATCF identifiers unique to each storm. The first two letters represent the basin (WP = Western Pacific, EP = Eastern Pacific, AL = North Atlantic, SH = Southern Hemisphere Basins), the first four numbers represent the season, and the last two numbers represent the ATCF storm number.

Table B. Storms used in the training, testing, and independent validation dataset. The first two letters represent the basin identifier. WP = Western Pacific, EP = Eastern Pacific, AL = North Atlantic, SH = Southern Hemisphere Basins. The next four numbers represent the season. The last two numbers are the ATCF storm number.

Training Dataset	Testing Dataset	Independent Validation
AL201614	AL201607	AL201715
AL201711	AL201712	AL201816
AL201714	AL201814	AL201905
AL201808	AL201913	EP201620
AL201806	EP201705	EP201810
AL201909	EP201817	EP201816
EP201613	SH201809	EP201911
EP201706	SH201907	SH201619
EP201802	SH201922	SH201815
EP201820	WP201630	SH201918
EP201803	WP201714	SH201912

Training Dataset	Testing Dataset	Independent Validation
EP201814	WP201822	WP201602
EP201807	WP201823	WP201616
EP201821	WP201910	WP201725
EP201913	WP201926	WP201810
EP201902	WP201902	WP201825
SH201611		WP201922
SH201718		WP201929
SH201807		
SH201811		
SH201913		
SH201906		
SH201920		
WP201621		
WP201625		
WP201612		
WP201707		
WP201720		
WP201831		
WP201826		
WP201828		
WP201830		
WP201911		
WP201924		
WP201920		
WP201915		

BIBLIOGRAPHY

Asano, J., and Coauthors, 2008: Analysis of tropical cyclones using microwave satellite imagery. RSMC Tokyo - Typhoon Cen. Tech. Rev. No. 10, 30–70, https://www.jma.go.jp/jma/jma-eng/jma-center/rsmc-hp-pub-eg/techrev/text10-3.pdf.

Cecil, D. J., and T Chronis, 2018: Polarization-corrected temperatures for 10-, 19-, 37-, and 89-GHz passive microwave frequencies. *J. Appl. Meteor. Climatol.*, **57**, 2249–2265, https://doi.org/10.1175/JAMC-D-18-0022.1.

DeMaria, M., and J. Kaplan, 1994: A statistical hurricane intensity prediction scheme (SHIPS) for the Atlantic Basin. *Wea. Forecasting*, **9**, 209–220, https://doi.org/10.1175/1520-0434(1994)009<0209:ASHIPS>2.0.CO;2.

DeMaria, M., C. R. Sampson, J. A. Knaff, and K. D. Musgrave, 2014: Is tropical cyclone intensity guidance improving?. *Bull. Amer. Meteor. Soc.*, **95**, 387–398, https://doi.org/10.1175/BAMS-D-12-00240.1.

Dvorak, V. F., 1984: Tropical cyclone intensity analysis using satellite data. NOAA Tech. Report NESDIS. 47 pp, https://repository.library.noaa.gov/view/noaa/19322.

Hawkins, J. D., and M. Helveston, T. F. Lee, F. J. Turk, K. Richardson, C. Sampson, J. Kent, and R. Wade, 2006: Tropical cyclone multiple eyewall configurations. *27th Conf. on Hurricanes and Trop. Meteor.*, Monterey, CA, Amer. Meteor. Soc., 6B.1, https://ams.confex.com/ams/27Hurricanes/techprogram/paper_108864.htm.

Hersbach, H., and Coauthors, 2020: The ERA5 global reanalysis. *Quart. J. Roy. Meteor. Soc.*, **146**, 1999–2049, https://doi.org/10.1002/qj.3803.

Irish, J. L., D. T. Resio, and J. J. Ratcliff, 2008: The influence of storm size on hurricane surge. *J. Phys. Oceanogr.*, **38**, 2003–2013, https://doi.org/10.1175/2008JPO3727.1.

Kaplan, J., and M. DeMaria, 2003: Large-scale characteristics of rapidly intensifying tropical cyclones in the North Atlantic basin. *Wea. Forecasting*, **18**, 1093–1108, https://doi.org/10.1175/1520-0434(2003)018<1093:LCORIT>2.0.CO;2.

Knaff, J. A., S. P. Longmore, and D. A. Molenar, 2014: An objective satellite-based tropical cyclone size climatology. *J. Climate*, **27**, 455–476, https://doi.org/10.1175/JCLI-D-13-00096.1.

Knaff, J. A., C. R. Sampson, and G. Chirokova, 2017: A global statistical–dynamical tropical cyclone wind radii forecast scheme. *Wea. Forecasting*, **32**, 629–644, https://doi.org/10.1175/WAF-D-16-0168.1.

Kossin, J. P., and M. DeMaria, 2016: Reducing operational hurricane intensity forecast errors during eyewall replacement cycles. *Wea. Forecasting*, **31**, 601–608, https://doi.org/10.1175/WAF-D-15-0123.1.

Kossin, J. P., and M. Sitkowski, 2009: An objective model for identifying secondary eyewall formation in hurricanes. *Mon. Wea. Rev.*, **137**, 876–892, https://doi.org/10.1175/2008MWR2701.1.

Lin, I. I., G. J. Goni, J. A. Knaff, C. Forbes, and M. M. Ali, 2012: Ocean heat content for tropical cyclone intensity forecasting and its impact on storm surge. *Nat. Hazards.* **66,** 1481–1500, https://doi.org/10.1007/s11069-012-0214-5.

Merrill, R. T., 1988: Environmental influences on hurricane intensification. *J. Atmos. Sci.*, **45**, 1678–1687, https://doi.org/10.1175/1520-0469(1988)045<1678:EIOHI>2.0.CO;2.

Mueller, K. J., M. DeMaria, J. Knaff, J. P. Kossin, and T. H. Vonder Haar, 2006: Objective estimation of tropical cyclone wind structure from infrared satellite data. *Wea. Forecasting*, **21**, 990–1005, https://doi.org/10.1175/WAF955.1.

NOAA, 2022: Fast Facts/Hurricane Costs. Accessed 18 March 2022, https://coast.noaa.gov/states/fast-facts/hurricane-costs.html.

Nordhaus, W. D., 2006: The economics of hurricanes in the United States. Natl. Bur. of Econ. Res. Work. Pap. Ser. Vol. 12813, 46 pp, https://doi.org/10.3386/w12813.

Powell, M. D., and T. A. Reinhold, 2007: Tropical cyclone destructive potential by integrated kinetic energy. Bull. Amer. Meteor. Soc., **88**, 513–526. https://doi.org/10.1175/BAMS-88-4-513.

Roebber, P. J., 2009: Visualizing multiple measures of forecast quality. *Wea. Forecasting*, **24**, 601–608.

Razin, M. N., C. J. Slocum, J. A. Knaff, P. J. Brown, and M. M. Bell, 2022: Tropical cyclone precipitation, infrared, microwave, and environmental database (TC PRIMED). *Bull. Amer. Meteor. Soc.*, **Accepted**.

Sampson, C. R., and A. J. Schrader, 2000: The Automated Tropical Cyclone Forecasting System (Version 3.2). *Bull. Amer. Meteor. Soc.*, **81**, 1231–1240, https://doi.org/10.1175/1520-0477(2000)081<1231:TATCFS>2.3.CO;2.

Sitkowski, M., J. P. Kossin, and C. M. Rozoff, 2011: Intensity and structure changes during hurricane eyewall replacement cycles. *Mon. Wea. Rev.*, **139**, 3829–3847, https://doi.org/10.1175/MWR-D-11-00034.1.

Slocum, C. J., M. N. Razin, J. A. Knaff, J. P. Stow, 2022: Does ERA5 mark a new era for resolving the tropical cyclone environment?. *J. Climate,* **Submitted.**

Virtanen, P., and others, 2020: SciPy 1.0: Fundamental algorithms for scientific computing in Python. *Nat. Methods*, **17**, 261–272, https://doi.org/10.1038/s41592-019-0686-2.

Wilks, D. S., 2019: Forecast verification. *Statistical methods in the Atmospheric Sciences* Elsevier, 369–483.

Willoughby, H. E., J. A., Clos, and M. G. Shoreibah, 1982: Concentric eye walls, secondary wind maxima, and the evolution of the hurricane vortex. *J. Atmos. Sci.*, **39**, 395–411, https://doi.org/10.1175/1520-0469(1982)039%3C0395:CEWSWM%3E2.0.CO;2.

Wimmers, A., 2018: Improved eyewall replacement cycle forecasting using a modified microwave-based algorithm (ARCHER). NOAA/OAR Joint Hurricane Testbed Final Report, 16 pp, https://www.nhc.noaa.gov/jht/15-17reports/Wimmers_197_progress_reportFINAL_113018.pdf.

ACADEMIC VITA

Alex Alvin Cheung | a98alvin@gmail.com or a98alvin@umd.edu

Objective

My goal is to gain a better understanding of the dynamical processes of the atmosphere, especially tropical cyclones, to improve numerical weather prediction.

Skills

- **Coding Skills:** MATLAB, Python
- **Teaching skills useful in a group setting:** Teaching Assistant, Tutor
- **Multilingual:** English, German (Goethe Certification B1), and Cantonese

Work History

Earth System Science REU at Colorado State University *Intern*, 05/2021 to 08/2021

- Under the mentorship of Drs. John Knaff and Chris Slocum, designed a secondary eyewall detection algorithm using machine learning.

National Weather Service State College WFO *Volunteer Intern*, 01/2021 to current

- Defined areas of radar utility in detecting snow squalls at varying ranges by combining NEXRAD-AWS radar data and PennDOT crash reports.

PA Climate Office *Intern*, 01/2020 to 05/2020; 01/2021 to 05/2021

- Designed a quality control algorithm for ingesting data in the new PA Mesonet.
- QC'd CoCoRaHS observations, authored climate highlights for the PA Climate Newsletter, and created interesting weather Tweets using SC-ACIS.

Introduction to Programming Techniques for Meteorology *Teaching Assistant* (METEO 273), 01/2021 to 05/2021

- Teaching introductory coding students proper coding etiquette and debugging support.
- Developing teaching and leadership skills in an academic setting.

Straube Foundation Education Blog *Manager*, 01/2016 to 08/2016; 05/2018 to 09/2019

- Three posts monthly to promote low-cost/cost-free technologies for education
- Goal is to help economically disadvantaged students acquire an affordable education

PSU Multicultural Resource Center *Tutor*, 09/2019 to current

- Provided a free tutoring service (Mainly Chemistry) to students in ethnic minorities and those that are underrepresented in STEM.

Education

Pennsylvania State University Schreyer Honors Scholar
Major: **Meteorology and Atmospheric Science (Department Marshal)**

Staffelsee Gymnasium- Murnau am Staffelsee, Germany 82418
Full-Year German American Partnership Program Exchange (2017-2018)

- Year-long exchange to a secondary school in Bavaria, Germany to learn German and German culture.

Involvement

PSU Weather Data Science Club (***president***), 08/2020 to 05/2022

- Coordinating an effort to upgrade and maintain the PSU Electronic Map Wall
- Creating a professional environment for students to develop practical coding skills for both operational meteorology and academia

Cellist at Penn State Campus Orchestra

Projects

1. **Detecting Tropical Cyclone Secondary Eyewalls using a Microwave-Based Scheme (Undergraduate Honors Thesis)** *(Presented at CSU REU Symposium as oral presentation and at AMS student conference as a Poster Session; Will present at AMS Tropical Meteorology Conference)*
2. **The Radius of Utility for Detecting Snow Squalls with Radar** *(Presented at NWA Conference (2nd place undergraduate poster) and at AMS as oral presentation)*
3. **An Evaluation of an Alternative Intensity Scale and the Extratropical Transition of Hurricane Sandy**
4. **Comparing Microphysical Properties of WRF Ensemble Data to Flight-Level Observations**
5. **PA Mesonet Quality Control Algorithm**

Awards

- **Meteorology and Atmospheric Science Department Marshal**
- **University of Maryland Flagship Graduate Fellowship**
- **American Meteorological Society Senior Scholarship (Naval Weather Service Association)**
- **Penn State Weather Information Technology Award**
  - Recognizes students who have contributed to the use of advanced technology in improved utilization of weather observations or numerical guidance for specialized forecast applications.
- **National Weather Association Conference (2021) 2nd Place Undergraduate Poster Presentation**

- *Quantifying Areas of Radar Utility for Snow Squall Detection in the NWS State College, PA County Warning Area*

Description of Research Experience

REU Project at CSU/CIRA: Detecting Tropical Cyclone Secondary Eyewalls using a Microwave-Based Scheme (Undergraduate Honors Thesis) *(Presented at CSU REU Symposium as oral presentation; Presented at AMS student conference: Poster Session; Will present at AMS Tropical Meteorology Conference as Oral Presentation)*

Intense tropical cyclones (TCs) often develop secondary eyewalls that can initiate a process known as an eyewall replacement cycle (ERCs). Eyewall replacement cycles can suddenly impact the intensity of TCs, as well as the internal structure and wind field. Currently, most of the scientific community's understanding of ERCs are based on research centered around the North Atlantic basin, due to the lack of aircraft reconnaissance data and an extensive climatology of ERCs in other basins globally. The REU portion of this project uses machine learning to recognize secondary eyewalls in TCs by combining a variety of environmental variables and satellite microwave imagery. In the undergraduate honors thesis portion, I am currently working on improving the reliability of this algorithm so that we can create an extensive ERC climatology that covers all basins around the globe.

National Weather Service Internship: Quantifying Areas of Radar Utility for Snow Squall Detection in the NWS State College, PA County Warning Area *(Presented at NWA Conference; Presented at AMS Conference as oral presentation)*

Snow squalls can often be characterized as shallow precipitation or lacking in vertical extent. As a result, when far from the radar, often, overshooting of the radar beam could underestimate or fail to detect such events. During my internship at the National Weather Service, I combined PennDOT crash data with NEXRAD-AWS radar archives to quantify ranges from the radar with various detection rates of impactful snow squalls. This project is slated to be implemented into the NWS Advanced Weather and Interactive Processing System this upcoming winter to help operational meteorologists while forecasting snow squalls. We are pursuing an NWS Eastern Region publication.

An Evaluation of an Alternative Intensity Scale and the Extratropical Transition of Hurricane Sandy

As part of an honors option with Dr. Steven Greybush, I authored a case study regarding the extratropical transition of Hurricane Sandy. In this project, I proposed an alternative integrated kinetic energy metric and compared it to Weather Research and Forecasting (WRF) model data during the transition. In this project, I learned how to properly write scientific papers and gained research skills for computer programming.

Comparing Microphysical Properties of WRF Ensemble Data to Flight-Level Observations

As part of an honors option with Dr. Steven Greybush and Dr. Matthew Kumjian, I authored a case study regarding the 5-8 February 2020 winter storm. In this project, I compared microphysical properties of NASA IMPACTS flight level data to WRF ensemble data to better identify the microphysical conditions of certain initial conditions that lead to better forecasts.

Description of Work Experience

PA State Climate Office Intern: PA Mesonet Quality Control Algorithm

As an intern with the Pennsylvania state climatologist, I quality controlled CoCoRaHS observations, authored climate highlights for the PA Climate Newsletter, and posted interesting weather tweets using SC-ACIS. In addition, I also developed a quality control algorithm that combines climatological norms and model output data to ingest data in the new PA Mesonet.

Introduction to Programming Techniques for Meteorology *Teaching Assistant* (METEO 273)

As a teaching assistant for Dr. Ying Pan, I helped students debug and learn proper coding etiquette and skills in MATLAB. This was an extremely rewarding experience because debugging other students' code provided me with valuable practice with reading code.